Analysis and optimization of cellular Kirigami wingbox (CKW) structures for enhanced aeroelastic performance

Mingzhi Huang
School of Engineering, Faculty of Engineering and Physical Sciences
University of Southampton, Southampton, SO17 1BJ, UK

Jie Yuan*
Computational Engineering Design Group
Faculty of Engineering and Physical Sciences
University of Southampton, Southampton, SO17 1BJ, UK
Email: j.yuan@soton.ac.uk

Harry Leith
Department of Mechanical and Aerospace Engineering
Faculty of Engineering
University of Strathclyde, Glasgow, G1 1XQ, United Kingdom

Fabrizio Scarpa
Bristol Composites Institute
School of Civil, Aerospace and Design Engineering (CADE), University of Bristol, Bristol, BS8 1TR, UK

Abstract

Cellular structures provide lightweight, high strength, and excellent structural stability due to their repetitive modular unit design. By integrating cutting and folding Kirigami techniques with composite and plastic substrates, cellular configurations can significantly enhance the aero-mechanical performance of wing designs. This innovative structural technology shows great promise for unmanned aerial vehicles (UAVs), enabling flexible control and dynamic flight capabilities to meet varying operational conditions. This study presents an analysis and optimization of the aeroelastic behaviour of cellular Kirigami wingbox (CKW) structures for multifunctional operations of micro-UAV wings to ensure stability and resilience in various dynamic flight conditions. The effect of thickness and internal cell angle of the cellular structure on static and dynamic aeroelastic behaviour is assessed through finite element analysis. By incorporating Bayesian optimization, the multidisciplinary design space of the cellular UAV wings has been efficiently explored to achieve optimal structural performance for adaptive UAV wings. The results show that Bayesian optimization effectively identifies optimal design parameters for different multi-objective design weights, which improves the aeroelastic performance of the CKW structure.

Nomenclature

t	core material thickness of CKW
h	cell height of CKW
l	cell length of CKW
θ	internal cell angle of CKW
EI	flexural stiffness
N	each normalized value
N_m	normalized value for wingbox mass
N_f	normalized value for flutter speed
N_d	normalized value for maximum deformation displacement
X	each computed value within the initial dataset
X_{best}	the best value among the initial dataset
X_{worst}	the worst value among the initial dataset
$f(\theta, t)$	Bayesian optimization objective function
m	the weight for wingbox mass
f	the weight for flutter speed
d	the weight for maximum deformation displacement

1.0 Introduction

Micro unmanned aerial vehicles (micro-UAVs) have become a focal point in aerospace research due to their small size, operational flexibility, and applicability in constrained or dynamic environments (Ahmed et al., 2022). Among them, morphing wing UAVs enable adaptive changes in wing geometry during flight, which can improve aerodynamic performance under varying flight conditions and expand mission capabilities (Barbarino et al., 2011). In the design of fixed-wing micro-UAVs, aspect ratios are commonly lower than those of full-scale aircraft, typically ranging from 1 to 4, to accommodate structural compactness, increase maneuverability, and improve gust response under low Reynolds number conditions (McMichael, 1997; Zufferey et al., 2006). Additionally, in small-scale and flexible wing structures, it is often observed that torsional, in-plane, and bending natural frequencies lie within a similar range due to the relatively uniform stiffness distribution and low mass, which can lead to mode coupling and reduced frequency separation (Livne, 2003; Wright & Cooper, 2008).

The cellular wingbox structure, inspired by natural honeycomb configurations, utilizes a lattice framework made from high-strength, lightweight materials, optimizing weight and strength. This structure's flexibility accommodates mechanical stresses from in-flight shape changes, maintaining structural integrity and aerodynamic efficiency (Heo et al., 2013). For the manufacturing of UAVs, additive manufacturing technology has been widely adopted due to its ability to utilize various materials to create lightweight structures with complex geometric shapes (Goh et al., 2017). However, Kirigami techniques hold a distinct advantage in terms of adaptively deforming according to aerodynamic demands. This advantage stems from their ability to introduce controlled hinge points within the material, which enable the structure to morph dynamically (Callens & Zadpoor, 2018; Zhai et al., 2021). The integration of the cellular wingbox structure with Kirigami techniques provides a cutting-edge approach for the design of morphing wing UAVs. This combination enhances flexibility and tailor-made mechanical properties, making it highly suitable for UAVs operating in diverse and demanding environments (Saito et al., 2011).

Aeroelastic analysis of the cellular Kirigami wingbox (CKW) structure constitutes a pioneering effort within the field. Prior to this, Li et al. (2023) had made a preliminary estimation of the divergence speed of CKW structures using analytic equations. Comparable aeroelastic studies include the research by Leitch et al. (2024) on continuous tow sheared

structures, Rivero et al. (2019) on fish bone active camber trailing edge devices, and Wang et al. (2018) on the application of round corrugated panels in the compliant structure. Conducting aeroelastic analysis on such an innovative structure as the CKW is crucial for ensuring structural integrity and operational safety. This encompasses both static aeroelasticity and flutter analysis. Static aeroelasticity evaluates how the wingbox structure deforms under steady aerodynamic forces. Flutter analysis explores the dynamic interactions between aerodynamic forces, structural elasticity, and inertia, which are essential for assessing the wingbox structure's resistance to destructive vibrations that could precipitate catastrophic failure. Collectively, these analyses are vital for defining safe operational thresholds and enhancing the reliability of the wingbox structure under diverse flight conditions, thus proving indispensable in the design process of the wingbox structure (Wright & Cooper, 2008).

The application of Bayesian optimization to the innovative design of the CKW structure enhances both the novelty and research value of this work. Utilizing Bayesian optimization for parameter tuning in CKW structures significantly enhances design efficiency and effectiveness. This optimization method leverages probabilistic models to predict and evaluate the performance of various design configurations, reducing the need for extensive physical testing. Compared to conventional strategies such as genetic algorithms, which often require a large number of function evaluations and are less sample-efficient, Bayesian optimization offers a more data-efficient and computationally economical approach. This is particularly beneficial when each design evaluation involves high-fidelity finite element simulations (Forrester et al., 2008; Shahriari et al., 2015; Snoek et al., 2012). Bayesian optimization has been widely applied in wing design; for example, Jim et al. (2021) optimized the wing design of supersonic aircraft using Bayesian optimization to effectively balance aerodynamic performance and reduce noise. In another study, Saporito et al. (2023) employed Bayesian optimization for the design of flexible aircraft, considering dynamic aeroelastic constraints such as flutter and gust loads, and uncertainties in wing structural parameters, providing optimized solutions with reliability assessments. Overall, applying Bayesian optimization to the design of the CKW structure provides an efficient solution for the high-fidelity design of complex wingboxes.

The aim of this paper is to efficiently search for optimal design parameters under different optimization criteria using Bayesian optimization, based on finite element analysis results of CKW with various structural parameters. To achieve this, the paper initially constructs wingbox models, detailing their geometrical parameterisation and finite element modelling. Notably, the wingbox structure will manifest as either hexagonal honeycomb or butterfly honeycomb depending on the sign of the internal cell angles. Hexagonal cells exhibit positive internal cell angles; reducing these angles decreases the Poisson's ratio of the honeycomb. Conversely, butterfly cells, with their negative internal cell angles, display a negative Poisson's ratio; stretching along one direction causes the honeycomb to expand perpendicular to the applied displacement. Subsequent numerical evaluations of different wingbox configurations include mesh sensitivity analysis, modal analysis, static aeroelastic analysis, and flutter analysis. These evaluations yield data on the wingbox's mass, deformation, and flutter speed sensitivities relative to the internal cell angle and cell material thickness. Ultimately, initial data under various internal angles and material thicknesses are utilized for Bayesian optimization, resulting in optimal internal angles and material thicknesses under different optimization criteria. The primary contribution of this work is demonstrating the aeroelastic advantages of CKW structures, such as structural stability and high flutter resistance. Additionally, it establishes the feasibility of applying Bayesian optimization to multi-objective, multidimensional design problems in high-fidelity, complex wingbox configurations.

2.0 Wingbox model

2.1 Geometrical parameterisation

The parameters defining the unit cell of centre-symmetric honeycomb configurations are described by Gibson and Ashby (1982). To enhance the efficiency and flexibility of the modeling process, Li et al. (2023) described Matlab/CAD processing method to perform Parametric Modeling techniques. The modelling approach enables the customization of honeycomb wingbox structures by considering input parameters like aerofoil chord length, wingbox width, distance from the core to leading and trailing edge, material thickness t, cell dimensions h and l, and the internal cell angle θ. Positive values of θ result in classical hexagonal and overexpanded honeycomb configurations, while negative values lead to butterfly honeycomb architectures with negative in-plane Poisson's ratios. The parameters t, l, h, and θ are illustrated in Figure 1.
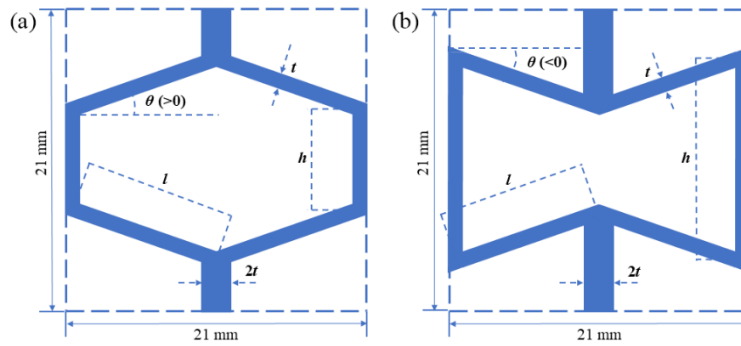
Figure 1. *2D geometry parameters: (a) hexagonal cell configuration, (b) butterfly cell configuration.*

The wingbox models in this study are constructed based on the NACA 2415 airfoil, which has been effectively utilized for low-speed MAVs (Genç et al., 2011; Saito et al., 2011; Soylak, 2016). Both the wing semi-span and chord length for this configuration are set at 0.14 m. The total height and total width of each individual unit cell are consistently maintained at 0.021 m, with a 5 mm distance from the cellular core to both the leading and trailing edges. The skin thickness is set to 1 mm. These values are adopted as preliminary design parameters to ensure structural strength under reasonable conditions (Li et al., 2023; Thill et al., 2008), and their further exploration within a multidimensional design space is planned for future work. As the internal cell angle θ changes, the lengths h and l are proportionally scaled to preserve the number of cells and the overall geometry of the wingbox. The orientation of the wingbox's chord length is consistent with the h dimension of the cells. The aerofoil and wingboxes with different cell configurations generated by the parametric modeling program are depicted in Figure 2. The study explores the impact of the internal cell angle θ within a range of $-40° \leq \theta \leq 40°$. The maximum and minimum values of θ are based on the largest and smallest angles possible before wall contact becomes an issue relative to the length l. The investigation into the influence of material thickness t spans a range from 0.2 mm to 0.8 mm, which falls within a structurally reliable engineering range for core material polyether-ether-ketone (PEEK) and has been widely adopted in Kirigami cellular structure studies (Chen et al., 2014; Del Broccolo et al., 2017; Li et al., 2023). The material thickness t is sampled at 0.2 mm intervals and the internal cell angle θ at 20° intervals to obtain a sufficiently diverse set of initial data points for Bayesian optimization. The design parameters explored in this research are summarized in Table 1.
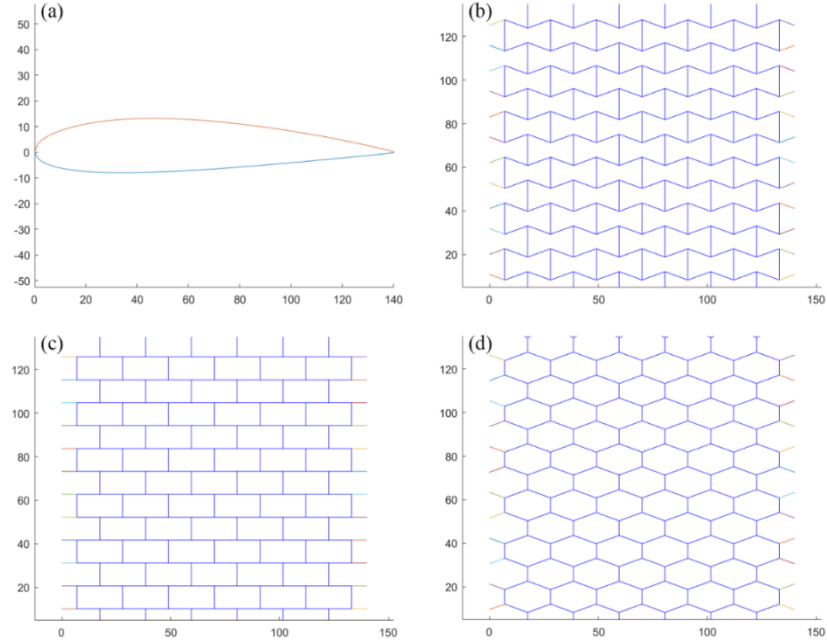
Figure 2. *The schematic of the wingbox structure generated by the parametric modeling program includes: (a) airfoil, (b) butterfly honeycomb configuration (θ = -20°), (c) rectangular honeycomb configuration (θ = 0°), (d) hexagonal honeycomb configuration (θ = 20°), axis units: mm.*

Table 1. *The design parameters of the baseline CKW architectures explored in this research*

Parameter	Value
Semi-span and chord length (mm)	140
Total height and width of each individual unit cell (mm)	21
Material thickness t (mm)	0.2, 0.4, 0.6, 0.8
Internal cell angle θ (°)	-40, -20, 0, 20, 40
Skin thickness (mm)	1
Distance from the core to the leading/trailing edge. (mm)	5

2.2 Finite element modelling

Scripts generated by parametric modeling in ANSYS Design Modeler are executed to create CKW models. After this initial creation, a skin conforming to the core of the wingbox is added. The model is then converted into a shell model due to the material thickness of wingbox being significantly smaller than other dimensions. This conversion enables the use of face meshing for both the core and skin of the wingbox, instead of body meshing, thereby reducing the number of elements and nodes, accelerating processing times, and enhancing the representation of structural behavior in thin-walled areas(Nguyen-Thanh et al., 2008). The finite element shell models of the wingbox with skin and the wingbox cores with different cell configurations are shown in Figure 3. As shown in Figure 3(a), the boundary conditions of the model are depicted with a fixed support set on the edge that would connect to the fuselage, to simulate the real wing scenario.
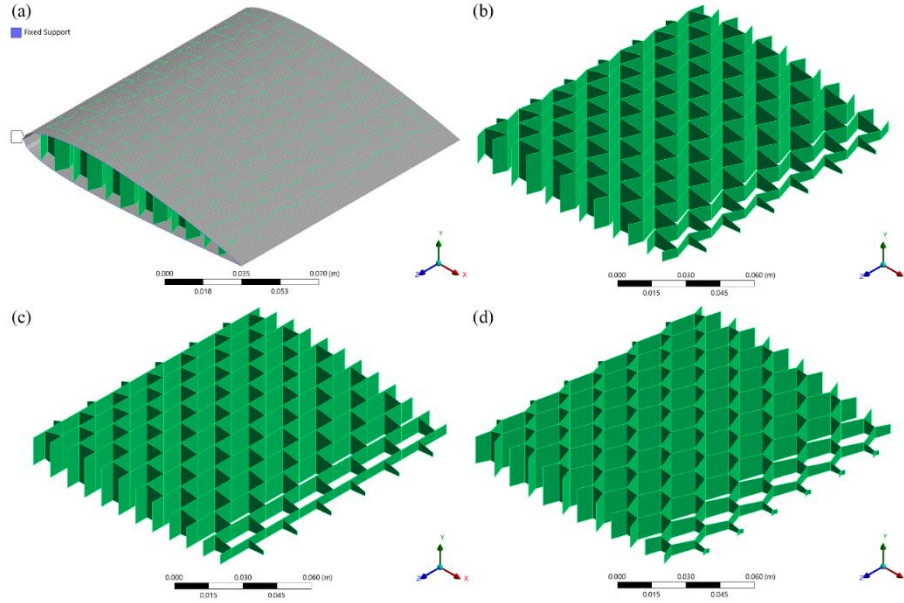
Figure 3. *CKW models: (a) with skin, (b) butterfly honeycomb configuration (θ = -20°), (c) rectangular honeycomb configuration (θ = 0°), (d) hexagonal honeycomb configuration (θ = 20°).*

Table 2. *Material properties of the CKW*

	Material	Young's modulus (MPa)	Poisson's ratio v	Density ρ (kg/m^3)
Wingbox core	PEEK	3950	0.393	1320
Skin	Silicone	2.83	0.48	1300

The core of the CKW utilizes PEEK due to its high strength-to-weight ratio, excellent wear resistance, and thermal stability. These properties enable the wingbox to achieve efficient aerodynamic performance and maintain structural integrity and durability under extreme environmental conditions (Flower & Soutis, 2003). The skin of the CKW is made from silicone elastomers, chosen for their high elongation at break and fatigue resistance, which provide the wingbox skin with effective deformation capabilities, ensuring structural integrity under fluctuating aerodynamic loads (Ahmad et al., 2022). The wingbox design using PEEK as the core material and silicone elastomers as the skin material demonstrated favorable mechanical properties in the studies conducted by Li et al. (2023). Material properties of the CKW are shown in Table 2.
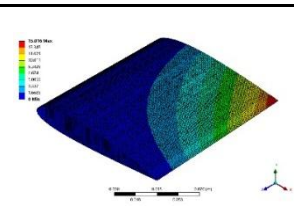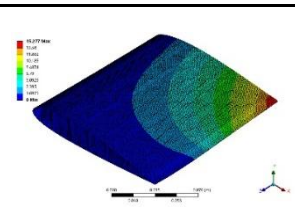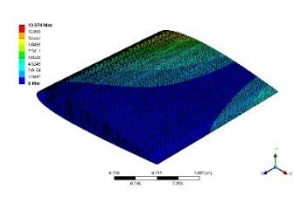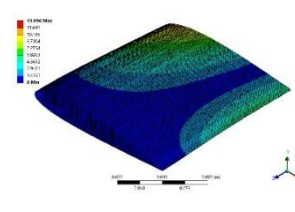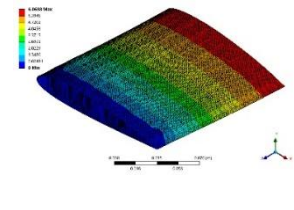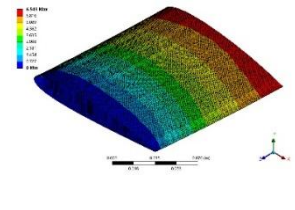
Following a mesh sensitivity analysis, where the modal analysis results were influenced by less than 1% due to changes in mesh size while minimizing the computational resources required, this study employs a meshing size of 1.2 mm as the standard. Additionally, rigid meshing is applied to the wingbox core to control mesh quality in the corner regions of the honeycomb walls, while flexible meshing is used for the skin to accommodate its curved structure and reduce computational resources.
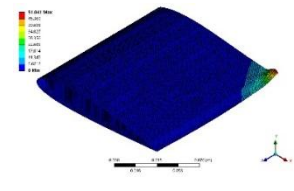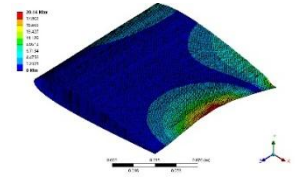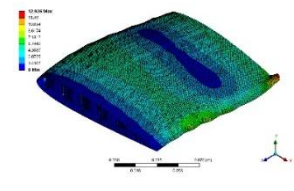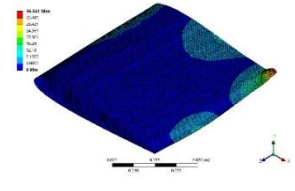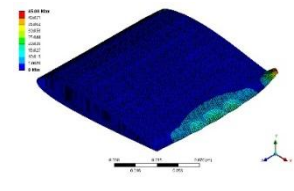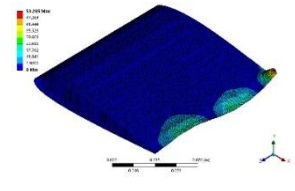
3.0 Numerical evaluation

3.1 Modal analysis

The modal analysis was performed in ANSYS. The results for the butterfly honeycomb configuration (θ = -20°) and hexagonal honeycomb configuration (θ = 20°), both with t = 0.2 mm, are presented in Table 3. The mode types and frequencies of the first three modes for both configurations are quite similar. The first mode is a first out-of-plane bending mode, with frequencies of 24.23 Hz for the butterfly configuration and 25.37 Hz for the hexagonal configuration. The second mode is a first torsion mode, with frequencies of 33.62 Hz and 32.32 Hz for the butterfly and hexagonal configurations, respectively. The third mode is a first in-plane bending mode, with frequencies of 39.65 Hz for the butterfly configuration and 46.53 Hz for the hexagonal configuration. The subsequent modes for both the butterfly honeycomb configuration and the hexagonal honeycomb configuration are all mixed modes, showing significant differences in mode types and frequencies. While the wingboxes in both configurations exhibit similarities in the lower-order modes, there are clear distinctions in the higher-order modes.

Table 3. *Modal analysis results for the first six modes of a CKW featuring butterfly honeycomb configuration (θ = -20°) and hexagonal honeycomb configuration (θ = 20°), both with t = 0.2 mm.*

Mode	Butterfly honeycomb (θ = -20°)		Hexagonal honeycomb (θ = 20°)	
	Plot	Frequency and Type	Plot	Frequency and Type
1st		24.23 Hz 1st out-of-plane bending		25.37 Hz 1st out-of-plane bending
2nd		33.62 Hz 1st torsion		32.32 Hz 1st torsion
3rd		39.65 Hz 1st in-plane bending		46.53 Hz 1st in-plane bending

4th		90.01 Hz Mixed		65.21 Hz Mixed
5th		117.68 Hz Mixed		78.66 Hz Mixed
6th		120.30 Hz Mixed		106.35 Hz Mixed

3.2 Static aeroelastic analysis

Static aeroelastic analysis was performed in Nastran using SOL 144 with the results visualized in Patran. The Doublet-Lattice Method (DLM) was utilized in aerodynamic modeling to supply the necessary aero loads for aeroelastic analyses (Demasi, 2024). In general, controlling the angle of attack between 0° and 6° can ensure the highest aerodynamic efficiency for UAVs (Liao et al., 2024). Kachel et al. (2022) compared six typical micro-UAVs, all of which have maximum speed ranging from 20 m/s to 28 m/s. This study initially conducted a static aeroelastic analysis on a CKW under the conditions of an air density of 1.226 kg/m³, with the flight speed set at 20 m/s and the angle of attack at 5°, both of which are considered reasonable for this analysis. The deformation displacement result of the CKW with the butterfly honeycomb configuration (θ = -20°, $t = 0.2\,mm$) is presented in Figure 4. The deformation displacement increases in the spanwise direction from the fixed support, with the maximum displacement of 1.71 mm occurring at the trailing edge of wing tip.
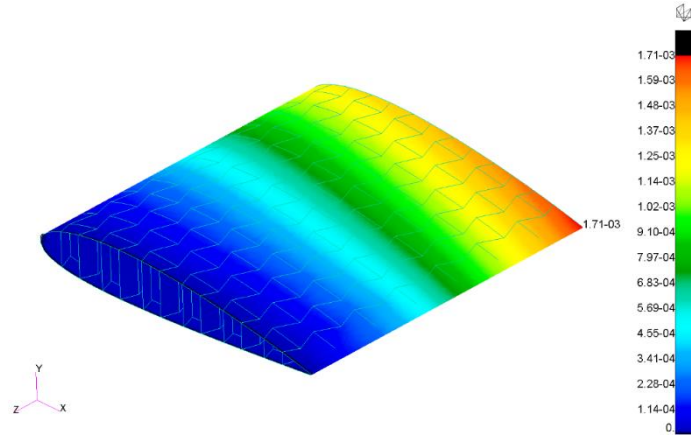
Figure 4. *Displacement Distribution of the CKW with butterfly honeycomb configuration (θ = -20°, t = 0.2 mm) under aerodynamic conditions of air density 1.226 kg/m³, flight speed 20 m/s, and angle of attack 5°, unit: mm.*
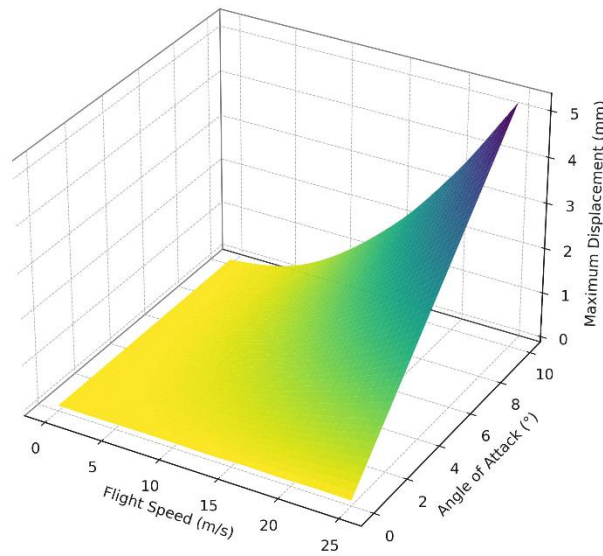

Figure 5. *Maximum displacement of the CKW with butterfly honeycomb configuration (θ = -20°, t = 0.2 mm) as a function of flight speed and angle of attack.*

To further expand the analysis on the ranges of flight speed and angle of attack, under aerodynamic conditions with air density maintained at 1.226 kg/m³, the flight speed was varied from 0 to 25 m/s, and the angle of attack ranged from 0° to 10°. The variation in maximum displacement of the CKW with the butterfly honeycomb configuration (θ = -20°, t = 0.2 mm) is shown in Figure 5. The maximum displacement exhibits a linear relationship with the angle of attack and an approximately quadratic relationship with the flight speed, as aligned as in the literature (Anderson, 2011). The peak displacement reaches approximately 5 mm, corresponding to a tip deflection of 3.57% relative to the semi-span of 140 mm. Given the elastic properties of the core material PEEK, this level of deformation remains within the expected linear-elastic range, thereby ensuring structural stability and preserving aerodynamic integrity (Solvay, 2015).

To investigate the effects of internal cell angle θ and material thickness t on the static aeroelastic performance of the CKW, Figure 6 illustrates the variation in maximum displacement of the CKW within the ranges of -40° ≤ θ ≤ 40° and 0.2mm ≤ t ≤ 0.8mm under

conditions of an air density of 1.226 kg/m³, a flight speed of 20 m/s, and an angle of attack of 5°. It can be observed that for configurations with the same θ, the maximum displacement decreases with increasing material thickness. This is primarily because an increase in thickness enhances the flexural stiffness EI of the wingbox, leading to smaller deformations under the same external load. However, for a constant material thickness, the wingbox configurations with different θ exhibit significant variations in deformation under the same external load.

Figure 7 presents the variation in total mass of the wingbox within the ranges of -40° $\leq \theta \leq$ 40° and 0.2mm $\leq t \leq$ 0.8mm. It can be observed that the mass of the wingbox decreases significantly with increasing θ. The butterfly honeycomb configuration requires less material compared to the hexagonal honeycomb configuration. However, the monotonic decrease in mass does not result in a monotonic reduction in EI. The butterfly honeycomb configuration, which has lower mass, exhibits better deformation resistance, whereas the rectangular honeycomb configuration demonstrates the poorest deformation resistance among the studied configurations. Nevertheless, Li et al. (2023) found that the rectangular honeycomb configuration of CKW exhibits the highest spanwise EI, which contradicts its poor resistance to deformation. This inconsistency arises because when the length walls fully align with the spanwise direction, it no longer contributes to EI in the chordwise direction. Consequently, this alignment leads to a decrease in chordwise EI, resulting in increased deformation at the trailing edge of the wing tip.
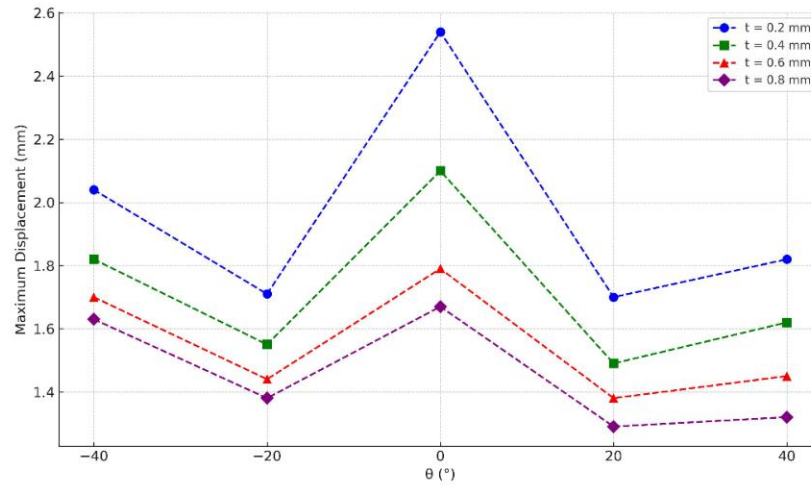

Figure 6. Maximum displacement of the CKW across internal cell angles θ and material thicknesses t under aerodynamic conditions of air density 1.226 kg/m³, flight speed 20 m/s, and angle of attack 5°.
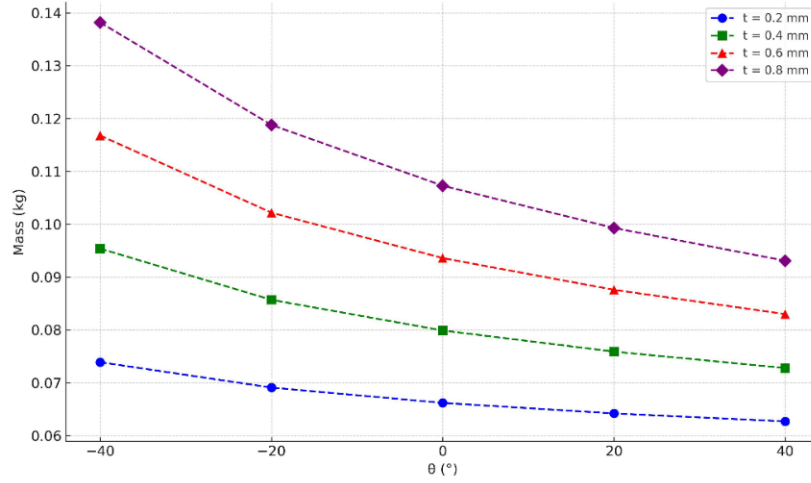
Figure 7. *Total mass of the CKW across internal cell angles θ and material thicknesses t.*

3.3 Flutter analysis

Flutter analysis was performed in NASTRAN using SOL 145. Figure 8(a) illustrates the variation in the natural frequencies of the first and second modes of the CKW for different internal cell angles θ as a function of flight speed, with a material thickness of $t = 0.2$ mm. It can be observed that, under the same flight speed, the natural frequency of the first mode is higher for configurations with $\theta = -20°$ and $\theta = 20°$. For the second mode, the natural frequency decreases from $\theta = -40°$ to $\theta = 0°$, then increases from $\theta = 0°$ to $\theta = 40°$. The natural frequency of the first mode increases with flight speed, while that of the second mode decreases, leading to modal coupling when the frequencies of the two modes converge. As shown in Figure 8(b), for all θ configurations of the CKW, the damping of the first two modes is slightly greater than zero at low speeds. As the flight speed increases, the damping of one of the modes decreases to negative upon modal coupling, at which point the vibrational energy of the system is no longer dissipated but accumulates with each vibration cycle. This accumulation causes the vibration amplitude to gradually increase, which ultimately leads to structural failure. This phenomenon marks the onset of flutter, with the flutter speed corresponding to the flight speed at which the damping becomes zero (Sudha et al., 2020).
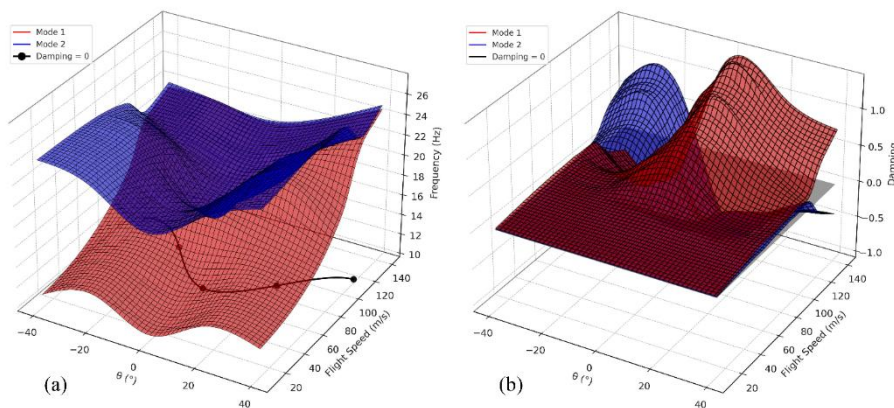

Figure 8. *The variation in (a) the natural frequencies and (b) the damping of the first and second modes of the CKW for different internal cell angles θ as a function of flight speed, with a material thickness of t = 0.2 mm.*

The curves where Damping = 0 in Figure 8(a) represent the relationship between flutter speed and θ. The flutter speed decreases initially with increasing θ, reaching a minimum value of 65 m/s at $\theta = 0°$, before increasing again. This flutter speed is significantly higher than the maximum speed of the six typical micro-UAVs investigated by Kachel et al. (2022), among which the fastest, the RQ-11 Raven, has a maximum speed of 27.8 m/s. This indicates that the CKW in this study has a substantial design margin for flight speed, providing ample design space for high-speed applications. Furthermore, Li et al. (2023) estimated the divergence speed of a CKW structure with comparable size and configuration using a theoretical expression (Megson, 2012), concluding that a structure with a 0.2 mm material thickness would diverge below 20 m/s. In contrast, the present study demonstrates that the wingbox encounters flutter prior to static divergence, and the predicted flutter speed exceeds 65 m/s, which is significantly higher than the value estimated by Li et al. This discrepancy may arise from the limitations of the theoretical formulation employed, which is derived under simplifying assumptions such as linear aerodynamic behavior, uniform torsional stiffness, and idealized beam models. These conservative assumptions are not fully applicable to the CKW configuration, which features complex geometry, distributed stiffness, and coupled deformation characteristics that are better represented through finite element modelling.

The variation in flutter speed of the wingbox within the ranges of -40° $\leq \theta \leq$ 40° and 0.2mm $\leq t \leq$ 0.8mm is shown in Figure 9. Under the same angle θ configuration, the flutter speed increases with increasing thickness because the increase in thickness enhances the *EI* of the wing box. Under the same thickness *t* configuration, the flutter speed decreases initially and then increases with increasing θ. The flutter speed reaches its minimum at $\theta = 0°$ and its maximum at $\theta = -40°$.
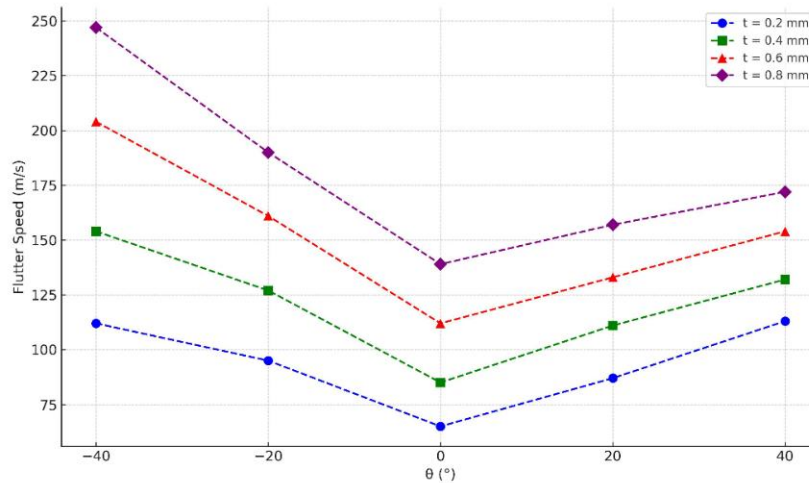

Figure 9. *Flutter speed of the CKW across internal cell angles θ and material thicknesses t.*

The influence of different honeycomb core materials on flutter speed was also investigated. In addition to PEEK and silicone, which were previously discussd, three additional materials commonly employed in flexible wing applications were considered for comparative analysis: carbon fiber reinforced polymer (CFRP) (Katagiri et al., 2020), Al 1050 alloy (Emad et al., 2022), and elastomer-glass fiber reinforced polymer (E-GFRP) (Mühlich et al., 2021). The analysis was conducted based on the butterfly honeycomb configuration with $\theta = -20°$ and $t = 0.2$ mm. As presented in Table 4, the results demonstrate a general positive correlation between flutter speed and the Young's modulus of the core material. This trend can be attributed to the fact that materials with higher stiffness enhance the bending and torsional rigidity of the wingbox, thereby increasing its natural frequencies and requiring greater aerodynamic loading, in terms of flight speed, to

induce flutter (Wright & Cooper, 2008). Nevertheless, when considering the overall structural mass, PEEK emerges as a particularly suitable core material due to its relatively low density while still maintaining sufficiently high flutter resistance.

Table 4. Material properties and corresponding flutter speeds for different core materials under butterfly honeycomb configuration ($\theta = -20°$, $t = 0.2\ mm$)

	CFRP	Al-1050	E-GFRP	PEEK	Silicone
Young's modulus (MPa)	150000	71000	17000	3950	2.83
Poisson's ratio v	0.28	0.33	0.30	0.393	0.48
Density ρ (kg/m³)	1580	2710	1850	1320	1300
Flutter speed (m/s)	162	147	113	95	62

4.0 Bayesian optimization

In this study, the bayesopt function in Matlab is utilized to perform Bayesian optimization on the internal cell angles θ and material thickness t of a CKW. The optimization ranges are set from $-40° \le \theta \le 40°$ and $0.2\ mm \le t \le 0.8\ mm$. The optimization objectives include minimizing mass, maximizing flutter speed, and minimizing maximum displacement under aerodynamic conditions with an air density of 1.226 kg/m³, flight speed of 20 m/s, and an angle of attack of 5°. In the objective function, the mass, flutter speed, and maximum displacement of the wingbox are normalized, with each objective scaled such that the best value is normalized to 0 and the worst value to 1 using the following equation:

$$N = \frac{X - X_{best}}{X_{worst} - X_{best}} \tag{1}$$

Where, N represents each normalized value, X denotes a computed value within the initial dataset as shown in Figures 7, 8, and 10, X_{best} indicates the best value among the initial dataset, and X_{worst} signifies the worst value. The Bayesian optimization objective function $f(\theta, t)$ is presented as follow:

$$f(\theta, t) = m \cdot N_m + f \cdot N_f + d \cdot N_d \tag{2}$$

Where, N_m, N_f, and N_d represent the normalized values for the wingbox mass, flutter speed, and maximum displacement, respectively. m, f, and d are the weights for the respective optimization objectives. To investigate the impact of prioritizing different design objectives on optimization outcomes, the weights for m, f, and d are considered in four distinct allocations: 1: 1: 1, 3: 1: 1, 1: 3: 1, and 1: 1: 3.

The results of the Bayesian optimization objective function model after 60 evaluations are shown in Figure 10, which effectively illustrates the shape of the predicted objective function under different weights and indicates the predicted point of the minimum value. Results of the objective values converge with the number of evaluations are shown in Figure 11. The estimated minimum values stabilize after approximately 10 evaluations. The estimated optimal minimum of $m: f: d = 1: 1: 1$ and 1: 1: 3 is located at $t = 0.8$ mm and $\theta = 40°$, with $f(\theta, t) = 0.839$ and 0.887. The estimated optimal minimum of $m: f: d = 3: 1: 1$ is located at $t = 0.2$ mm and $\theta = 40°$, with $f(\theta, t) = 1.161$. The estimated optimal minimum of $m: f: d = 1: 3: 1$ is located at $t = 0.8$ mm and $\theta = -40°$, with $f(\theta, t) = 1.278$. Under varying priority objective weights, different optimal design parameters emerge. These optimization results converge at the endpoints of the optimization range, indicating that the best solutions are constrained by the boundaries of the optimization space. Figure 12 displays Pareto points for multi-objective optimization, showcasing the optimal design solutions within the optimization range under different objective weights.
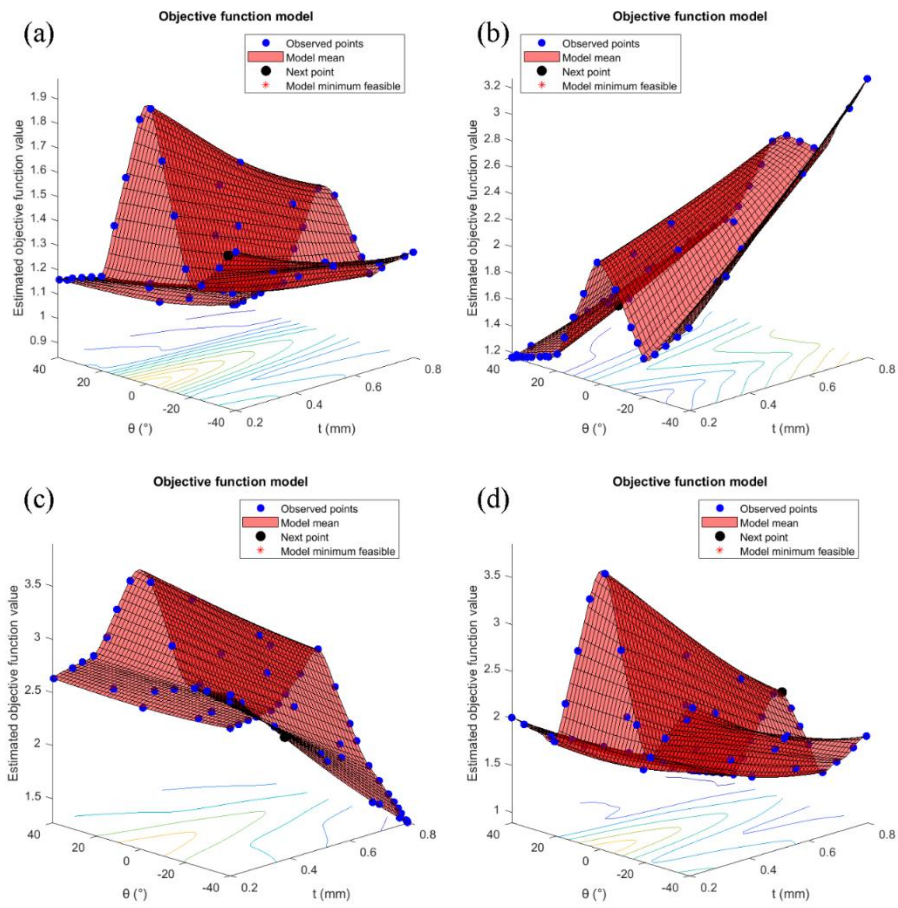
Figure 10. *Results of the Bayesian optimization objective function model after 60 evaluations for different* ṁ : ḟ : ḋ *: (a) 1: 1: 1, (b) 3: 1: 1, (c) 1: 3: 1, (d) 1: 1: 3.*
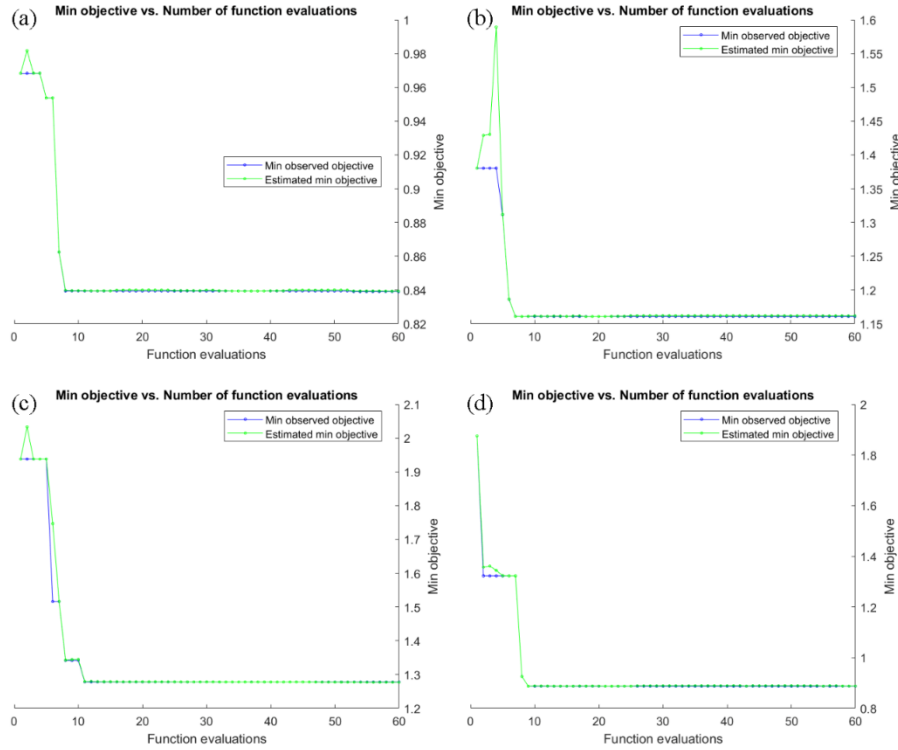
Figure 11. *Results of the objective values converge with the number of evaluations for different $m: f: d:$ (a) 1: 1: 1, (b) 3: 1: 1, (c) 1: 3: 1, (d) 1: 1: 3.*
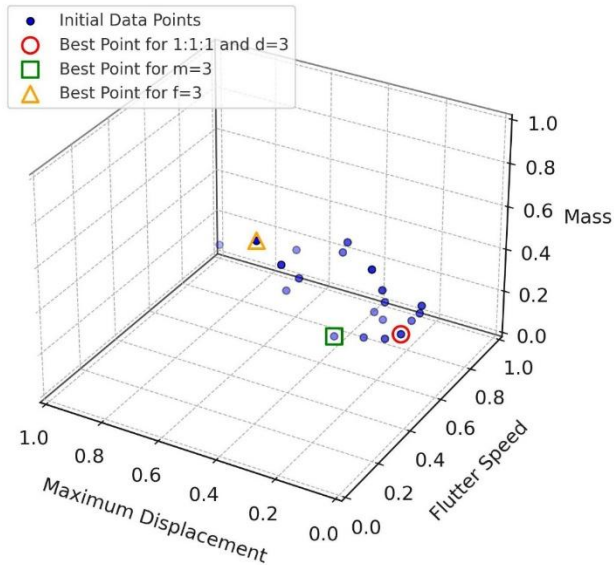

Figure 12. *Pareto points of initial dataset and optimized best points under different objective weights.*

Given that the minimum flutter speed in the initial dataset is 65 m/s, which is substantially higher than the typical maximum flight speed of micro-UAVs, a flutter speed of 65 m/s is deemed to provide adequate safety margins. Therefore, within the optimization ranges, the flutter speed is consistently within acceptable limits and is no longer considered in the optimization objectives. The new Bayesian optimization objective function is defined as $f(\theta, t) = N_m + N_d$, considering only the impact of wingbox mass and maximum displacement. The results of this optimization objective function model after 60 evaluations,

and the convergence of objective values with the number of evaluations, are shown in Figure 13. The estimated minimum values stabilize after 26 evaluations. The estimated optimal minimum is located at $t = 0.313$ mm and $\theta = 20.1°$, with $f(\theta, t) = 0.341$. This represents a predicted best point that is distinct from any initial data point and does not reside at the edge of the optimization ranges. New simulation for a wingbox model at $t = 0.31$ mm and $\theta = 20°$ yields a mass of 0.0706 kg and a maximum displacement of 1.57 mm. The corresponding normalized values are 0.105 for mass and 0.224 for maximum displacement, with an objective function value of 0.329. The Pareto points for mass and maximum displacement are displayed in Figure 14. The optimized best point is located on the Pareto Front and is closer to the origin than all initial data points. The best objective function value in the initial dataset is located at $t = 0.4$ mm and $\theta = 20°$, with a value of 0.335. After Bayesian optimization, the new best objective function value is 0.329, an improvement of approximately 1.8%. When considering a scenario closer to reality, without the influence of sufficiently high flutter speeds, Bayesian optimization effectively improves the design parameters of the CKW, making $t = 0.31$ mm and $\theta = 20°$ the new optimal design parameters.
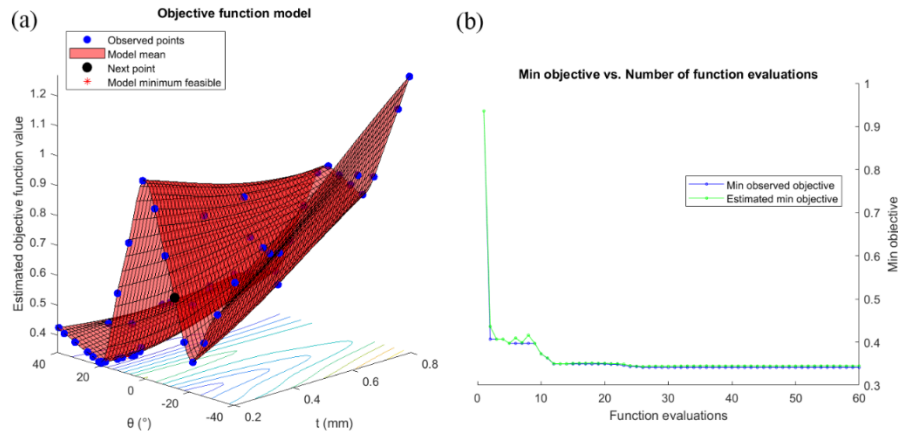

Figure 13. *Results of (a) Bayesian optimization objective function $f(\theta, t) = N_m + N_d$ model after 60 evaluations and (b) objective values converge with the number of evaluations. The minimum value is 0.341 at $t = 0.313$ mm and $\theta = 20.1°$.*

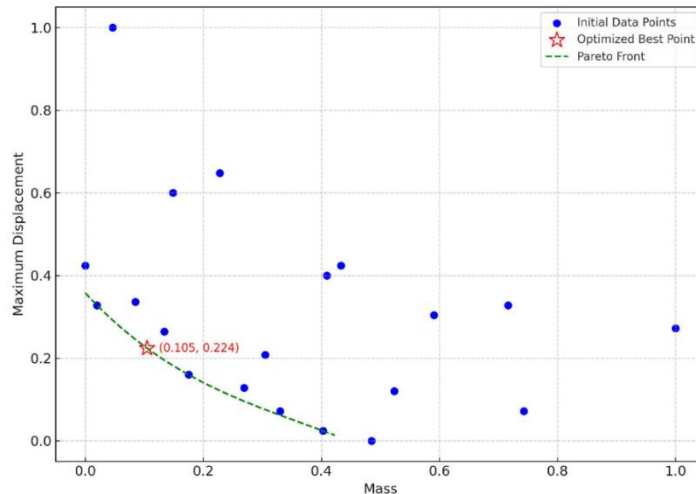**Figure 14.** *Pareto points and optimized best point of the Bayesian optimization objective function $f(\theta, t) = N_m + N_d$.*

5.0 Conclusion

This study advances the aeroelastic analysis and optimization of CKW structures. Through finite element modeling and extensive numerical evaluations, it highlights the effects of internal cell angles θ and material thickness t on the aeroelastic properties of CKW for micro-UAV applications. The mass of the wingbox significantly decreases with increasing θ. The deformation resistance of the wingbox increases with t but varies non-monotonically with θ; the rectangular honeycomb configuration exhibits the least deformation resistance, while the hexagonal honeycomb configuration at $\theta = 20°$ shows the strongest. In terms of flutter speed for the wingbox, the performance of the butterfly honeycomb configuration is slightly better than that of the hexagonal honeycomb configuration and significantly superior to the rectangular honeycomb configuration.

Building on this, the study effectively employed Bayesian optimization to search for optimal design parameters aimed at balancing minimizing mass, minimizing deformation, and maximizing flutter speed. The results indicate that under different design objective weights, there are various optimal parameter configurations, allowing for customization based on specific requirements. The study also conducted optimization under the more realistic assumption that a flutter speed of 65 m/s is sufficiently safe, predicting optimal aeroelastic performance at $t = 0.31$ mm and $\theta = 20°$. Finite element results align with this prediction, showing a performance improvement of approximately 1.8% over the best initial data. This research demonstrates that CKW structures possess sufficient structural stability to maintain aerodynamic integrity under loading conditions, and that their favorable flutter characteristics may support high-speed or maneuvering flight scenarios. Furthermore, the integration of Bayesian optimization provides a practical framework for multi-objective optimization in multidimensional design spaces for high-fidelity complex wingbox structures.

Acknowledgements

References

Ahmad, D., Ajaj, R. M., & Amoozgar, M. (2022). Elastomer-based skins for morphing aircraft applications: Effect of biaxial strain rates and prestretch. *Polymer Testing*, *113*, 107655. https://doi.org/10.1016/j.polymertesting.2022.107655

Ahmed, F., Mohanta, J., Keshari, A., & Yadav, P. S. (2022). Recent advances in unmanned aerial vehicles: a review. *Arabian Journal for Science and Engineering*, *47*(7), 7963-7984. https://doi.org/10.1007/s13369-022-06738-0

Anderson, J. (2011). *EBOOK: Fundamentals of Aerodynamics (SI units)*. McGraw hill.

Barbarino, S., Bilgen, O., Ajaj, R. M., Friswell, M. I., & Inman, D. J. (2011). A review of morphing aircraft. *Journal of intelligent material systems and structures*, *22*(9), 823-877. https://doi.org/10.1177/1045389X11414084

Callens, S. J., & Zadpoor, A. A. (2018). From flat sheets to curved geometries: Origami and kirigami approaches. *Materials Today*, *21*(3), 241-264. https://doi.org/10.1016/j.mattod.2017.10.004

Chen, Y., Scarpa, F., Remillat, C., Farrow, I., Liu, Y., & Leng, J. (2014). Curved Kirigami SILICOMB cellular structures with zero Poisson's ratio for large deformations and morphing. *Journal of intelligent material systems and structures*, *25*(6), 731-743.

Del Broccolo, S., Laurenzi, S., & Scarpa, F. (2017). AUXHEX–A Kirigami inspired zero Poisson's ratio cellular structure. *Composite Structures*, *176*, 433-441.

Demasi, L. (2024). *Introduction to Unsteady Aerodynamics and Dynamic Aeroelasticity*. Springer.

Emad, D., Mohamed, A., & Fanni, M. (2022). Modeling and flight control of small UAV with active morphing wings. *Journal of Intelligent & Robotic Systems*, *106*(2), 42.

Flower, H. M., & Soutis, C. (2003). Materials for airframes. *The Aeronautical Journal*, *107*(1072), 331-341. https://doi.org/10.1017/S0001924000013658

Forrester, A., Sobester, A., & Keane, A. (2008). *Engineering design via surrogate modelling: a practical guide*. John Wiley & Sons.

Genç, M. S., Kaynak, Ü., & Yapici, H. (2011). Performance of transition model for predicting low Re aerofoil flows without/with single and simultaneous blowing and suction. *European Journal of Mechanics-B/Fluids*, *30*(2), 218-235. https://doi.org/10.1016/j.euromechflu.2010.11.001

Gibson, I., & Ashby, M. F. (1982). The mechanics of three-dimensional cellular materials. *Proceedings of the royal society of London. A. Mathematical and physical sciences*, *382*(1782), 43-59. https://doi.org/10.1098/rspa.1982.0088

Goh, G. D., Agarwala, S., Goh, G. L., Dikshit, V., Sing, S. L., & Yeong, W. Y. (2017). Additive manufacturing in unmanned aerial vehicles (UAVs): Challenges and potential. *Aerospace Science and Technology*, *63*, 140-151. https://doi.org/10.1016/j.ast.2016.12.019

Heo, H., Ju, J., & Kim, D.-M. (2013). Compliant cellular structures: application to a passive morphing airfoil. *Composite Structures*, *106*, 560-569. https://doi.org/10.1016/j.compstruct.2013.07.013

Jim, T. M., Faza, G. A., Palar, P. S., & Shimoyama, K. (2021). Bayesian optimization of a low-boom supersonic wing planform. *AIAA Journal*, *59*(11), 4514-4529. https://doi.org/10.2514/1.J060225

Kachel, S., Okoń, T., Frant, M., & Majcher, M. (2022). Project for a reconnaissance unmanned aerial vehicle. *Journal of KONBiN*, *52*(3), 187-200. https://doi.org/10.2478/jok-2022-0032

Katagiri, K., Yamaguchi, S., Kawakita, S., Honda, S., Sasaki, K., Kogiso, N., & Tamayama, M. (2020). Fabrication of the twist morphing wing for the UAV by CFRP with applying the electrodeposition resin molding method. AIAA Scitech 2020 Forum,

Leitch, H. J., Yuan, J., & Stodieck, O. (2024). Effect of Thickness Variation on the Aeroelastic Performance of Continuous Tow Sheared Structures. In *AIAA SCITECH 2024 Forum*. https://doi.org/10.2514/6.2024-0191

Li, Q., Ainsworth, O., Allegri, G., Yuan, J., & Scarpa, F. (2023). Assessing the mechanical and static aeroelastic performance of cellular Kirigami wingbox designs. *Aerospace Science and Technology*, *143*, 108716. https://doi.org/10.1016/j.ast.2023.108716

Liao, Y., Cheng, K., Sun, W., Zhao, Y., Jia, X., & Qi, W. (2024). Computational fluid dynamics analysis of aerodynamic characteristics in long-endurance unmanned aerial vehicles. *Heliyon*, *10*(19). https://doi.org/10.1016/j.heliyon.2024.e38804

Livne, E. (2003). Future of airplane aeroelasticity. *Journal of Aircraft*, *40*(6), 1066-1092.

McMichael, J. M. (1997). Micro air vehicles-toward a new dimension in flight. *http://www. arpa. gov/tto/MAV/mav_auvsi. html*.

Megson, T. H. G. (2012). *Aircraft structures for engineering students*. Elsevier.

Mühlich, M., González, E. A., Born, L., Körner, A., Schwill, L., Gresser, G. T., & Knippers, J. (2021). Deformation behavior of elastomer-glass fiber-reinforced plastics in dependence of pneumatic actuation. *Biomimetics*, *6*(3), 43.

Nguyen-Thanh, N., Rabczuk, T., Nguyen-Xuan, H., & Bordas, S. P. (2008). A smoothed finite element method for shell analysis. *Computer Methods in Applied Mechanics and Engineering*, *198*(2), 165-177. https://doi.org/10.1016/j.cma.2008.05.029

Rivero, A. E., Weaver, P., Cooper, J., & Woods, B. K. S. (2019). Progress on the design of a composite FishBAC morphing device for spanwise lift control. 22nd International Conference on Composite Materials: ICCM22, Melbourne, Victoria, Australia.

Saito, K., Agnese, F., & Scarpa, F. (2011). A cellular kirigami morphing wingbox concept. *Journal of intelligent material systems and structures*, *22*(9), 935-944. https://doi.org/10.1177/1045389X11416030

Saporito, M., Da Ronch, A., Bartoli, N., & Defoort, S. (2023). Robust multidisciplinary analysis and optimization for conceptual design of flexible aircraft under dynamic aeroelastic constraints. *Aerospace Science and Technology*, *138*, 108349. https://doi.org/10.1016/j.ast.2023.108349

Shahriari, B., Swersky, K., Wang, Z., Adams, R. P., & De Freitas, N. (2015). Taking the human out of the loop: A review of Bayesian optimization. *Proceedings of the IEEE*, *104*(1), 148-175.

Snoek, J., Larochelle, H., & Adams, R. P. (2012). Practical bayesian optimization of machine learning algorithms. *Advances in neural information processing systems*, *25*.

Solvay. (2015). KetaSpire PEEK Design & Processing Guide. In: Solvay Brussels, Belgium.

Soylak, M. (2016). Experimental investigation of aerodynamic performance of oscillating wings at low Re numbers. *Proceedings of the Institution of Mechanical Engineers, Part G: Journal of Aerospace Engineering*, *230*(10), 1882-1902. https://doi.org/10.1177/0954410015619646

Sudha, U. P. V., Deodhare, G. S., & Venkatraman, K. (2020). A comparative assessment of flutter prediction techniques. *The Aeronautical Journal*, *124*(1282), 1945-1978. https://doi.org/10.1017/aer.2020.84

Thill, C., Etches, J., Bond, I., Potter, K., & Weaver, P. (2008). Morphing skins. *The Aeronautical Journal*, *112*(1129), 117-139.

Wang, C., Khodaparast, H. H., Friswell, M. I., & Shaw, A. D. (2018). Compliant structures based on stiffness asymmetry. *The Aeronautical Journal*, *122*(1249), 442-461. https://doi.org/10.1017/aer.2017.144

Wright, J. R., & Cooper, J. E. (2008). *Introduction to aircraft aeroelasticity and loads* (Vol. 18). John Wiley & Sons.

Zhai, Z., Wu, L., & Jiang, H. (2021). Mechanical metamaterials based on origami and kirigami. *Applied Physics Reviews*, *8*(4). https://doi.org/10.1063/5.0051088

Zufferey, J.-C., Klaptocz, A., Beyeler, A., Nicoud, J.-D., & Floreano, D. (2006). A 10-gram microflyer for vision-based indoor navigation. 2006 IEEE/RSJ International Conference on Intelligent Robots and Systems,